RECENT PROGRESS IN INTENSE VORTEX RADIATION SOURCES AT SXFEL

X. R. Zhu[1,2], C. L. Li[3], Y. Kang*[3], C. Feng†[3], Z. T. Zhao[3]
[1]Shanghai Institute of Applied Physics, Chinese Academy of Sciences, Shanghai, China
[2]University of Chinese Academy of Sciences, Beijing, China
[3]Shanghai Advanced Research Institute, Chinese Academy of Sciences, Shanghai, China

Abstract

Vortex radiation carries orbital angular momentum (OAM) and is attractive for applications including chiral characterization, magnetic imaging, and ultrafast light–matter interaction studies. A scheme for vortex radiation generation and diagnostics at the Shanghai Soft X-ray Free-Electron Laser facility (SXFEL) based on wavefront shaping of a 266 nm external seed laser is studied. Three-dimensional simulations with realistic SXFEL parameters show clear annular intensity and helical phase distributions, with the peak power of about 448 MW at the radiator exit for the representative working point. The proposed diagnostics further enable clear identification and characterization of the generated OAM radiation. The results support the feasibility of controlled vortex radiation generation at SXFEL and its future extension to shorter wavelengths.

INTRODUCTION

Radiation carrying OAM, or vortex radiation, has a helical wavefront, an on-axis phase singularity, and a hollow transverse intensity profile. These features enable coupling to angular-momentum degrees of freedom and make vortex radiation useful for chiral-structure identification, magnetic-order imaging, nanoscale angular-momentum transport, and ultrafast nonequilibrium studies [1–4].

Free-electron lasers (FELs) provide high brightness, ultrashort, and tunable coherent radiation, making them promising sources of intense vortex beams. Proposed FEL-based OAM schemes include seeded FELs, FEL oscillators, and self-seeding configurations [5–9]. Seeded FELs are especially attractive because an external seed laser allows flexible phase control and harmonic up-conversion. Motivated by the wavefront-shaping method for high-gain FEL vortex generation [10], this paper studies its implementation at SXFEL using a 266 nm seed laser, with emphasis on realistic simulations and experimentally accessible diagnostic signatures.

The remainder of this paper is organized as follows. In Section 2, the basic principle of the proposed technique is introduced. Section 3 presents the simulation results. Section 4 presents the diagnostic method and criterion. Finally, concluding remarks are given in Section 5.

* kangy@sari.ac.cn
† fengc@sari.ac.cn

SCHEME

A wavefront shaping unit is introduced into the seeded FEL platform at SXFEL so that the 266 nm seed laser obtains the required transverse phase before entering the modulator, as shown in Fig. 1. The shaped seed imprints an azimuth-dependent energy modulation on the electron beam; the dispersive section converts it into helical density modulation; and the radiator amplifies the corresponding vortex microbunching. The shaping concept uses two planar mirrors with a small relative angle.

Following the wavefront-tilt scheme, the seed field at the modulator entrance is [10]

$$E_s(x,y) = E_{\mathrm{G}}(x,y)\exp[ik_s\alpha x\ \mathrm{sgn}(y)]\,, \tag{1}$$

where E_{G} is the Gaussian envelope, $k_s = 2\pi/\lambda_s$, and α is the effective wavefront tilt. In the beam–laser overlap region, $k_s\alpha x\,\mathrm{sgn}(y)$ can approximate the target azimuthal phase $l\theta$.

In the modulator, the seed induces an energy modulation [5, 11, 12]

$$\Delta\gamma(r,\theta,s) = \frac{eK_m JJ L_m}{2\gamma mc^2}E_s(r)\sin(k_s s + l\theta + \phi_0), \tag{2}$$

where K_m and L_m are the dimensionless undulator parameter and effective length of the modulator, respectively, JJ is the planar undulator coupling factor, γ is the relativistic Lorentz factor of the electron beam, s is the longitudinal coordinate, and ϕ_0 is the initial phase. After the dispersive section, the density modulation becomes

$$\rho = \rho_0\left[1 + 2\sum_{n=1}^{\infty}|b_n|\cos(nk_s s + nl\theta + \psi_n)\right], \tag{3}$$

with average charge density ρ_0, harmonic bunching factor b_n, and phase ψ_n. For HGHG, the helical bunching at the nth harmonic is [5, 11]

$$b_n(r,\theta) = e^{-B^2n^2/2}J_n(-nAB)\,e^{inl\theta}, \tag{4}$$

where $A = \Delta E/\sigma_E$ and $B = k_s R_{56}\sigma_E/E_b$. Thus the radiator tuned to the selected harmonic amplifies microbunching carrying the seed-imposed azimuthal phase.

SIMULATION RESULTS OF THE PRESENT SCHEME

The feasibility of the present SXFEL scheme was evaluated with three-dimensional GENESIS 1.3 simulations [13].

PREPRINT

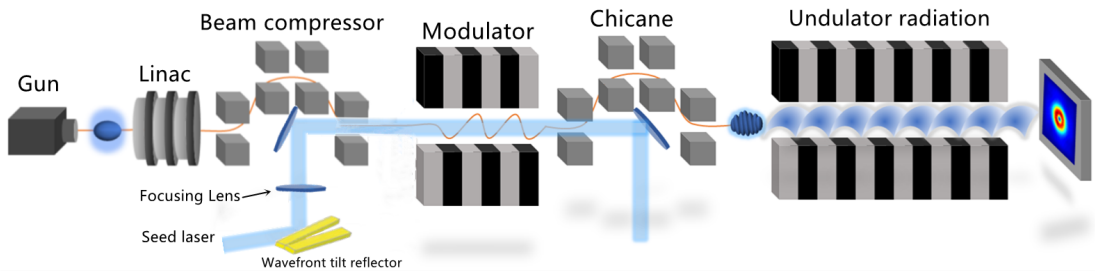

Figure 1: Schematic layout of the proposed vortex radiation generation scheme at SXFEL.

Table 1: Representative Simulation Parameters Used in this Paper

Parameter	Value
External seed laser wavelength	266 nm
Harmonic number	1
Output radiation wavelength	266 nm
Electron beam energy	0.77 GeV
Bunch length / charge	267 fs / 500 pC
Normalized emittance	0.4 μm·rad
Slice energy spread	51.1 keV rms
Modulator period / periods	68 mm / 58
R_{56}	0.4 mm
Radiator period / periods	80 mm / 16

A representative fundamental working point was selected, so the harmonic number is $n = 1$ and the output wavelength is 266 nm. The main parameters are listed in Table 1.

Figure 2 shows the longitudinal evolution of the peak power and azimuthal-mode bunching factors.The peak power reaches about 448 MW, or 0.45 GW, at the radiator exit. The $n = 1, l = -1$ bunching grows from about 0.365 to 0.446, while the $l = 0$ component remains nearly zero and the $l = 1$ component stays much lower, indicating dominant amplification of the target vortex mode.

Figure 3 shows the output transverse intensity and phase. The annular intensity profile and continuously winding phase confirm the expected OAM-carrying radiation. Together with Eq. (4), the result shows that the seed-imposed azimuthal phase is preserved through modulation, dispersion, and FEL amplification.

DIAGNOSTIC METHOD AND CRITERION

A multipinhole far field interference method can provide a practical way to identify vortex modes [14]. This approach does not rely on complex optics such as lenses or beam splitters for short-wavelength radiation; instead, it uses the phase superposition of multiple coherent sub-beams at the imaging plane to reveal the topological charge of the incident beam.

The geometrical configuration of the multipinhole far-field interference method is illustrated in Fig. 4. An incident beam is sampled by an N-pinhole circular array on the micropore-array plane, where the nth pinhole is located at the azimuthal angle α_n. The diffracted sub-beams then propagate to the imaging plane and interfere at the observation point (X, Y, Z). For an incident field carrying topological charge l, each sampled sub-beam acquires an additional azimuth-dependent phase. As a result, the morphology of the far-field interference pattern becomes directly related to the OAM mode of the incident radiation.

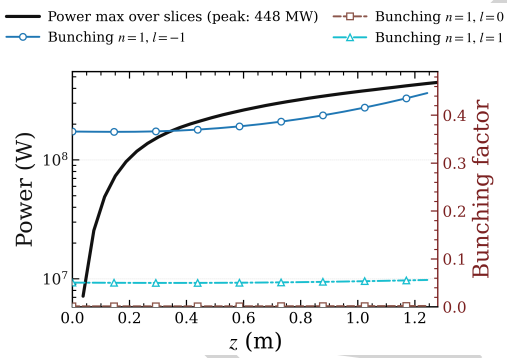

Figure 2: Longitudinal evolution of the peak power and bunching factors of different azimuthal modes along the radiator.

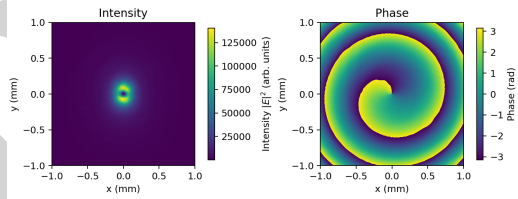

Figure 3: Transverse intensity (left) and phase (right) distributions of the output radiation at the radiator exit.

For a circular array composed of N pinholes, the far-field interference intensity can be written as [14]

$$I_l^N(x, y, z) \propto \left| \sum_{n=1}^{N} \exp\left[-il\alpha_n - \frac{ika}{z}\left(x\cos\alpha_n + y\sin\alpha_n\right)\right]\right|^2 . \tag{5}$$

where $k = 2\pi/\lambda$ is the radiation wavenumber, a is the radius of the pinhole array, $\alpha_n = 2\pi n/N$ is the azimuthal angle of the nth pinhole, and z is the propagation distance from the multipinhole plane to the imaging plane. Equation (5) indicates that the far-field interference pattern is determined

PREPRINT

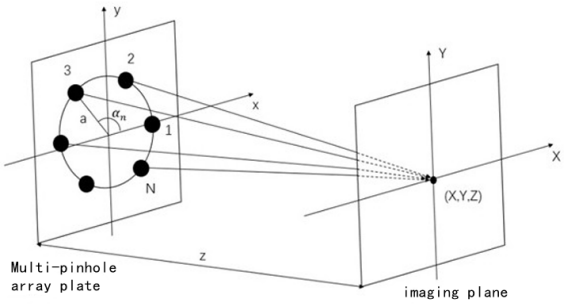

Figure 4: Geometrical configuration of the multipinhole far-field interference method. The incident beam is sampled by an N-pinhole circular array on the micropore-array plane, and the diffracted sub-beams interfere at the imaging plane after a propagation distance z.

not only by the array geometry but also directly by the additional phase factor $\exp(-il\alpha_n)$, and therefore can be used to distinguish different OAM modes.

Figure 5: Reference and simulated far-field interference patterns used for mode discrimination. Left: Gaussian-like beam with $l = 0$, showing a circular bright-spot array. Middle: vortex beam with $l = -1$, showing a hexagonal-like pattern [14]. Right: multipinhole far-field interference pattern calculated from the GENESIS output field in the present work.

Figure 5 presents the reference and simulated patterns adopted here for mode discrimination. The left panel corresponds to a Gaussian-like output with $l = 0$, while the middle panel corresponds to a vortex output with $l = -1$ [14]. In addition, the right panel shows the far-field interference pattern calculated from the output optical field obtained in the present GENESIS simulations by applying the same multipinhole diagnostic principle. The resulting pattern exhibits a nontrivial polygonal bright-spot distribution rather than the circular spot arrangement characteristic of the $l = 0$ case, and it is qualitatively consistent with the vortex-mode reference pattern.

Combined with the annular transverse intensity profile and the continuously winding phase distribution already shown in Fig. 3, the simulated diagnostic result in the right panel of Fig. 5 provides an additional and more experimentally relevant signature of the generated OAM state. Therefore, if a measured multipinhole far-field interference pattern in the future experiment resembles the simulated pattern and remains consistent with the $l = -1$ reference morphology, it would serve as a direct criterion for confirming the successful generation and identification of the target vortex mode in the present scheme.

CONCLUSION

This paper investigates a complete scheme for vortex radiation generation and diagnostics based on wavefront-shaped 266 nm seed laser manipulation at SXFEL.

Three-dimensional numerical simulations with realistic machine parameters show that the present scheme can produce output radiation with clear vortex characteristics, including an annular transverse intensity profile and a continuously winding helical phase structure, while the peak power reaches about 448 MW at the radiator exit for the representative working point. In addition, the proposed diagnostic method provides a practical way to distinguish the target vortex mode with $l = -1$ from a Gaussian-like mode through its characteristic far field interference pattern.

These results establish a robust technical basis for controlled investigations of vortex radiation at SXFEL and provide a practical pathway for extending the present wavefront-shaped seeding scheme from the demonstrated 266 nm fundamental case to higher-harmonic and shorter-wavelength vortex radiation.

ACKNOWLEDGEMENTS

Valuable support in FEL physics, wavefront shaping, diagnostic design, and numerical simulations is gratefully acknowledged.

REFERENCES

[1] L. Allen, M. W. Beijersbergen, R. J. C. Spreeuw, and J. P. Woerdman, "Orbital angular momentum of light and the transformation of Laguerre–Gaussian laser modes", *Phys. Rev. A*, vol. 45, no. 11, pp. 8185–8189, 1992. doi:10.1103/PhysRevA.45.8185

[2] S. Sasaki and I. McNulty, "Proposal for generating brilliant X-ray beams carrying orbital angular momentum", *Phys. Rev. Lett.*, vol. 100, no. 12, p. 124801, 2008. doi:10.1103/PhysRevLett.100.124801

[3] L. Ye, Jérémy. R. Rouxel, S. Asban, B. Rösner, and S. Mukamel, "Probing molecular chirality by orbital-angular-momentum-carrying X-ray pulses", *J. Chem. Theory Comput.*, vol. 15, no. 7, pp. 4180–4192, 2019. doi:10.1021/acs.jctc.9b00346

[4] M. Fanciulli *et al.*, "Observation of magnetic helicoidal dichroism with extreme ultraviolet light vortices", *Phys. Rev. Lett.*, vol. 128, no. 7, p. 077401, 2022. doi:10.1103/PhysRevLett.128.077401

[5] E. Hemsing, A. Marinelli, and J. B. Rosenzweig, "Generating optical orbital angular momentum in a high-gain free-electron laser at the first harmonic", *Phys. Rev. Lett.*, vol. 106, no. 16, p. 164803, 2011. doi:10.1103/PhysRevLett.106.164803

[6] E. Hemsing and A. Marinelli, "Echo-enabled X-ray vortex generation", *Phys. Rev. Lett.*, vol. 109, no. 22, p. 224801, 2012. doi:10.1103/PhysRevLett.109.224801

PREPRINT

[7] Pž. Rebernik Ribič, D. Gauthier, and G. De Ninno, "Generation of coherent extreme-ultraviolet radiation carrying orbital angular momentum", *Phys. Rev. Lett.*, vol. 112, no. 20, p. 203602, 2014. doi:10.1103/PhysRevLett.112.203602

[8] N. Huang and H. Deng, "Generating X-rays with orbital angular momentum in a free-electron laser oscillator", *Optica*, vol. 8, no. 7, pp. 1020–1023, 2021. doi:10.1364/OPTICA.428341

[9] J. Yan and G. Geloni, "Self-seeded free-electron lasers with orbital angular momentum", *Adv. Photonics Nexus*, vol. 2, no. 3, p. 036001, 2023. doi:10.1117/1.APN.2.3.036001

[10] Z. Zhou, Y. Kang, W. Wan, and C. Feng, "Intense X-ray vortices generation via wavefront shaping in high-gain free-electron lasers", *Phys. Rev. Lett.*, vol. 134, no. 20, p. 205001, 2025. doi:10.1103/PhysRevLett.134.205001

[11] L. H. Yu, "Generation of intense UV radiation by subharmonically seeded single-pass free-electron lasers", *Phys. Rev. A*, vol. 44, no. 8, pp. 5178–5193, 1991. doi:10.1103/PhysRevA.44.5178

[12] E. Hemsing, G. Stupakov, D. Xiang, and A. Zholents, "Beam by design: laser manipulation of electrons in modern accelerators", *Rev. Mod. Phys.*, vol. 86, no. 3, pp. 897–941, 2014. doi:10.1103/RevModPhys.86.897

[13] S. Reiche, "GENESIS 1.3: a fully 3d time-dependent FEL simulation code", *Nucl. Instrum. Methods Phys. Res. A*, vol. 429, no. 1–3, pp. 243–248, 1999. doi:10.1016/S0168-9002(99)00114-X

[14] C. Li, B. Li, C. Feng, H. Sun, and B. Liu, "Vortex-light diagnostic device for a free-electron laser facility", Chinese Patent Application, China, No. CN119374742A, Jan. 2025.

PREPRINT